A Comparative Study of Ground-level Enhancement Events of Solar Energetic Particles

Leon Kocharov[1] , Alexander Mishev[1,2], Esa Riihonen[3], Rami Vainio[3] , and Ilya Usoskin[1,2]

[1] Sodankylä Geophysical Observatory, University of Oulu, Oulu 90014, Finland
[2] Space Physics and Astronomy Research Unit, Faculty of Sciences, University of Oulu, Oulu 90014, Finland
[3] Space Research Laboratory, Department of Physics and Astronomy, University of Turku, Turku 20014, Finland

Abstract

Major solar eruptions can accelerate protons up to relativistic energies. Solar relativistic ions arriving at 1 au may cause a solar particle event detectable by the worldwide network of neutron monitors (NMs), a ground-level enhancement (GLE) event. Using the newly computed NM yield function, we have fitted the 15 historic GLEs. Moments of the fitted proton distributions are used for the analysis. Profiles of the proton net flux are very diverse, while some profiles are similar. For this study, we select two events with similar time profiles, GLE 60 (2001 April 15) and GLE 65 (2003 October 28), and ask what makes these GLEs similar. We compare the GLEs with their progenitor solar flares and coronal mass ejections (CMEs). We find a close relationship between the rise and peak of the GLE, on the one hand, and the solar flare and the metric radio emissions from extended coronal sources at the base of the CME, on the other hand. The GLE decay time, the rate of the proton spectrum evolution, and the CME speed are proportional to the duration of the soft X-ray flare. We compare the two GLEs with GLE 59 (2000 July 14) analyzed by Klein et al. and with the deka-MeV nucleon^{-1} proton and helium data from the ERNE instrument on the Solar and Heliospheric Observatory spacecraft. The comparison indicates that a single solar eruption can produce more than one component of solar energetic particles, differently contributing at different energies and locations.

1. Introduction

The energy range of protons emitted by solar eruptions, flares, and coronal mass ejections (CMEs) into the interplanetary medium may extend in the strongest events up to the rigidities/energies $\sim$1–10 GV/$\sim$ 433 MeV–9.1 GeV (Dorman 2004 and references therein). Accelerated ions with energy >300 MeV nucleon^{-1} can generate a nuclear cascade in the Earth's atmosphere, the byproducts of which can eventually be registered by ground-based detectors such as neutron monitors (NMs), causing a ground-level enhancement (GLE) event (Shea & Smart 1982).

The solar proton parameters obtained from the NM network data change during the event, so that two components of GLEs have been defined: a prompt component (PC) and a delayed component (DC; e.g., Vashenyuk et al. 1997). A GLE event starts with the PC, whose spectrum is hardest at around 1 GV but gets steeper at higher rigidities. The proton angular distribution typically indicates an anisotropic particle flux arriving from the Sun. The DC becomes dominant after $\sim$ 1–2 hr and has a softer spectrum at 1 GV, which is close to a single power law in the NM-observed rigidity range. Resolving the GLE sources is still a complicated issue (Nitta et al. 2012). In this paper, we will focus on the properties and possible origins of the GLE's PC, and we do not study the DC.

For the goals of the GLE data analysis, the worldwide network of NMs is considered as a single instrument placed on the rotating platform that is the Earth (Bieber & Evenson 1995). Such an "instrument" includes also the Earth's magnetosphere and atmosphere, which "collimate" the solar particle flux and convert it into the secondaries to be detected by NMs. For the interpretation of the GLE data, we use a wide set of the solar and solar wind data. The instruments and data employed in this research are described in Section 2. In Section 3, we review the newly fitted GLEs and select two of them for a detailed study. The two selected GLEs are compared with data of the solar electromagnetic observations and data of the deka-MeV nucleon^{-1} proton and helium registration with the ERNE instrument on the Solar and Heliospheric Observatory (SoHO), respectively, in Sections 4 and 5.

2. Instrumentation and Data

The spectral and angular characteristics of the solar relativistic protons can be deduced from the records of the worldwide network of ground-based NMs if a relationship is established between the NM count rates and the primary particles in the interplanetary space, which requires a modeling of the particle transport and interaction in the Earth's magnetosphere and atmosphere, and a fitting of an actual set of the observed NM count-rate profiles with a model solar particle distribution outside the magnetosphere (Debrunner & Brunberg 1968; Hatton 1971; Debrunner & Lockwood 1980; Shea & Smart 1982; Cramp et al. 1997; Clem & Dorman 2000; Dorman 2004; Desorgher et al. 2009; Mishev & Usoskin 2013). The NM network data can be retrieved from the GLE database hosted at the University of Oulu.[4] Details of the adopted fitting procedure are given in Section 3.1 and the Appendix.

We use also the solar energetic particle (SEP) data in the deka-MeV nucleon^{-1} range. Differential proton and helium measurements in narrow energy channels with a good

---

[4] https://gle.oulu.fi

resolution in the proton arrival directions are from the High Energy Detector (HED) of SoHO/ERNE (Torsti et al. 1995). SoHO is a stabilized platform orbiting outside the Earth's magnetosphere around the Lagrange point L1, in the solar wind upstream of the Earth.

The transport of SEPs may proceed in different interplanetary magnetic field (IMF) structures. We acquire the solar wind data from in situ measurements by the SoHO/CELIAS/MTOF Proton Monitor (Hovestadt et al. 1995) and the IMF data from the Advanced Composition Explorer (ACE) spacecraft, which, like SoHO, orbits in the solar wind upstream of the Earth around the point L1. The magnetic field is measured by the Magnetometer instrument (MAG; Smith et al. 1998). The data are provided by the ACE Science Center.[5] An identification of the near-Earth interplanetary coronal mass ejections (ICMEs) has been done by Richardson and Cane (Cane & Richardson 2003; Richardson & Cane 2010).[6]

To learn the GLE origins, we need data of solar electromagnetic observations. The soft X-ray data are from the GOES satellites, including solar images from the Solar X-ray Imager (SXI) on board GOES 12 (Pizzo et al. 2005). The EUV images are from SoHO/Extreme ultraviolet Imaging Telescope (EIT; Delaboudiniere et al. 1995). Here we use the 195 Å derotated difference images produced by the Novel EIT wave Machine Observing (NEMO) software package (Podladchikova & Berghmans 2005) from the NEMO EIT Waves and Eruptive Dimmings Catalog.[7]

The CME images are from the SoHO coronagraphs. For the heliocentric distance range ∼2.25–7 $R_\odot$, the images are from the C2 coronagraph, and farther from the Sun, they are from C3, parts of the Large Angle and Spectrometric COronagraph (LASCO; Brueckner et al. 1995). We also use data from the LASCO CME catalog generated and maintained at the CDAW Data Center by NASA and the Catholic University of America, in cooperation with the Naval Research Laboratory (Yashiro et al. 2004).[8]

In the radio band, the meter wavelength images of the Sun are obtained from the Nançay Radioheliograph (NRH) in France, which operates at five frequencies—164, 237, 327, 410, and 435 MHz, with a spatial resolution of ∼3′ at 164 MHz (Kerdraon & Delouis 1997). We also inspect the radio dynamic spectra at decimeter wavelengths from the radio spectrograph and the data of the 3 GHz radiometer, both operated by the Astronomical Institute in Ondrejov, Czech Republic (Jiricka et al. 1993), and the 25–180 MHz spectrograms from the San Vito Solar Observatory, which is part of the USAF Radio Solar Telescope Network.[9] At low frequencies, below 13.8 MHz, dynamic radio spectra are available from the WAVES instrument on board the Wind spacecraft (Bougeret et al. 1995). We use also the Wind/WAVES type II bursts catalog[10] (Gopalswamy et al. 2019), as well as the optical and radio data from different observatories summarized in the Solar Geophysical Data by the NOAA National Geophysical Data Center in Boulder, Colorado.[11]

---

[5] http://www.srl.caltech.edu/ACE/ASC/

[6] https://izw1.caltech.edu/ACE/ASC/DATA/level3/icmetable2.htm

[7] https://www.sidc.be/nemo/

[8] https://cdaw.gsfc.nasa.gov

[9] https://www.ngdc.noaa.gov/stp/space-weather/solar-data/solar-features/solar-radio/rstn-spectral/

[10] https://cdaw.gsfc.nasa.gov/CME_list/radio/

[11] https://www.ngdc.noaa.gov/stp/solar/sgd.html

3. GLE Events

3.1. Analysis Method

In GLE studies, the distribution of high-energy solar protons is described by their intensity per unit of rigidity, P. The rigidity spectrum is modeled with a modified power law—that is, the negative exponent of the power law in rigidity may linearly decrease with increasing rigidity—if the data require a steepening of the proton spectrum (similar to Cramp et al. 1997). It is assumed that the angular distribution is axially symmetric, fitted with the Gaussian function, so the proton intensity outside the magnetosphere is of the form:

$$j(P, \theta, t) = j_o \, e^{-\theta^2/\sigma^2}(P/P_o)^{-\gamma - \delta\gamma[(P/P_o)-1]}, \quad (1)$$

where the pitch angle θ is measured from the symmetry axis of the intensity distribution; $P_o = 1$ GV. The axis direction, the angular distribution width σ, the spectral parameters γ and $\delta\gamma$, and the parallel intensity j_o of the 1 GV protons are functions of time to be determined in the course of a fitting procedure. Some more details of the procedure and the fitted parameters for two selected GLEs are given in the Appendix.

For the goals of the present work, we further employ the moments of the fitted proton distribution. The zero-order moment of the proton intensity distribution $j(P, \theta, t)$ is the omnidirectional intensity:

$$J(P, t) = 2\pi \int_0^\pi j(P, \theta, t)\sin\theta \, d\theta. \quad (2)$$

The omnidirectional intensity is proportional to the number density of protons with rigidity P:

$$N(P, t) = J(P, t)/v(P), \quad (3)$$

where $v(P)$ is the proton speed.

The next moment is the net flux of the protons at the Earth's orbit:

$$S(P, t) = 2\pi \int_0^\pi j(P, \theta, t)\cos\theta\sin\theta \, d\theta. \quad (4)$$

Hereafter, we adopt the vector $\boldsymbol{S}$ pointing in the direction of the proton stream, which is opposite to an "instrument" viewing direction, which will be $-\boldsymbol{S}$. The time profile of the net flux is the most relevant to the history of the proton production at the Sun. The average pitch-angle cosine of the protons arriving at 1 a.u. is

$$\langle\cos\theta\rangle = S(P, t)/J(P, t). \quad (5)$$

It characterizes the proton streaming, which depends on the interplanetary transport conditions and the event's phase.

The last employed moment is the cumulative net flux of energy up to a current time, i.e., the fluence of energy of >1 GV solar protons passing the Earth orbit:

$$Q(t) = \int_0^t d\tau \int_{1\,\text{GV}}^\infty dP \, E(P)S(P, \tau). \quad (6)$$

It serves as a measure of the total power of the GLE and the relative power of its phases.

3.2. Event Selection

We have reviewed in terms of the distribution moments a total of 15 newly fitted GLEs. Their net flux profiles are shown in Figure 1. The spectral-steepening parameter $\delta\gamma$, defined by
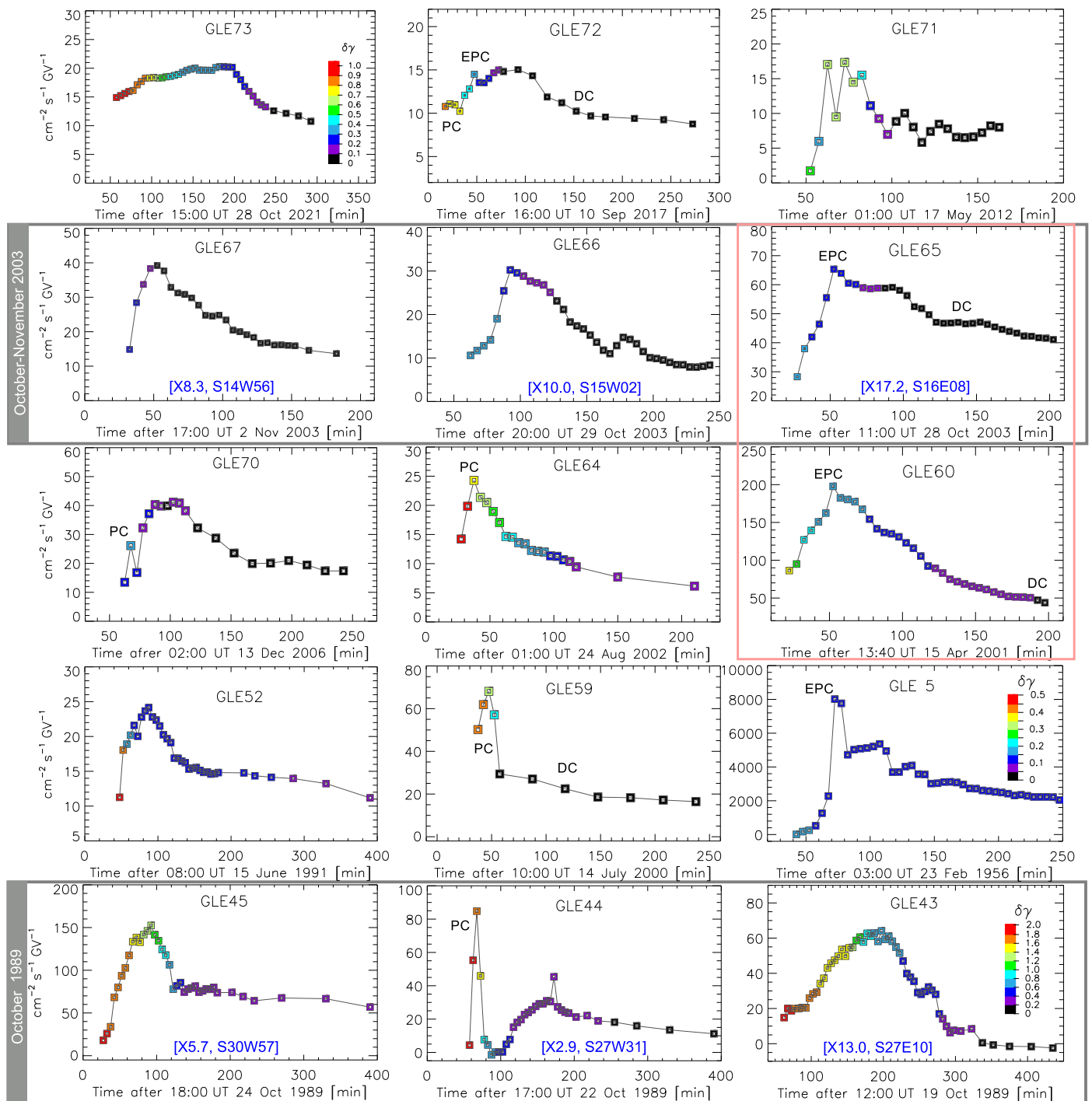
Figure 1. Time profiles of the 1 GV proton flux, S, of the 15 newly analyzed GLEs. The value of the spectral parameter $\delta\gamma$ is indicated by the point colors. The three outlined panels of the second row (GLE 65, GLE 66, and GLR 67) and the three panels of the lowermost row (GLE 43, GLE 44, and GLE 45) are for the two series of GLEs each originating from a single complex of the solar ARs in 2003 October–November and in 1989 October, respectively (the solar coordinates of the associated flares and their magnitudes are indicated in the panels). The two GLEs selected for the present comparative study are outlined in orange. The $\delta\gamma$ color bar shown in the GLE 73 panel applies to all other panels, except those for which an alternate color bar is defined (GLE 5 and the 1989 series). The extended prompt component (EPC) will be defined in Section 6.1.

Equation (1), is indicated by the point colors. The events include in particular the historic GLE 5, on 1956 February 23, the well-known GLE 59, on 2000 July 14 (the Bastille Day event), and the most recent GLE 73, on 2021 October 28. There are two GLE series originating from a fixed active region (AR) during its transit across the solar disk: the 2003 series that includes GLEs 65, 66, and 67 on October 28, 29, and

November 2, respectively, and the 1989 series comprising GLEs 43, 44, and 45 on October 19, 22, and 24.

There is a wide variety of GLE profile shapes in Figure 1, while some profiles look the same qualitatively. After the visual inspection, we have selected for a comparative study two GLEs, GLE 60, on 2001 April 15, and GLE 65, on 2003 October 28, whose flux profiles are surprisingly similar to each

other, even though they do not belong to the same GLE series. Fortunately, both events occurred not too long ago and at nearly the same time of day, so similar data sets are available for the associated solar flares and CMEs from instruments installed on SoHO, ACE, and Wind and in the same observatories on the ground. Then the question can be raised: which phenomena of solar activity in these two eruptions coincide and, therefore, could be crucial for the proton acceleration to relativistic energies and escape to the solar wind? Note that the strongest ever GLE 5, on 1956 February 23, is of the same morphological type as the two selected GLEs, but in that era, there were no opportunities for modern multiwavelength observations.

3.3. GLE 60 versus GLE 65: High-energy Protons and Solar Wind

Time profiles of the proton flux S of GLE 60 (2001 April 15) and GLE 65 (2003 October 28) are plotted in the uppermost panels of Figures 2 and 3, respectively. Both events have a moderately steep rise phase, ending with a sharp peak followed by a two-step decline. In panels (d), we plot the GSE coordinate angles, latitude ψ and longitude λ, of the symmetry axis of the proton intensity distribution, in the direction opposite to the proton flux, $-S$. The IMF intensity and the IMF direction angles are shown in panels (b) and (c). The IMF parameters are measured on board ACE near the L1 point, so for a comparison with the GLE data, they are shifted in time for the solar wind transit time from the ACE orbit to the orbit of the Earth. In panels (c), the R_L bar additionally illustrates the passage time of a solar wind structure of the Larmor radius scale of 1 GV proton, R_L/U, where U is the solar wind speed. Abrupt changes in the IMF direction on the scale of $(1–2)R_L$ can cause high-energy protons to decouple from the magnetic field lines, thereby facilitating their cross-field transport (see Kocharov et al. 2020 for more discussion of the cross-field transport and references).

Three periods of the GLE events and three corresponding streams of solar wind can be distinguished: Period/Stream M at $t_1 < t < t_2$, Period/Stream I at $t_2 < t < t_3$, and Period/Stream L at $t > t_3$ (Figures 2 and 3). The GLE's Main (M) period includes the event's rise, maximum, and early decay phase. In this period of both events, the high-energy protons arrive predominantly along the lines of the relatively stable magnetic field (panels (e) and (c)). The IMF is also stable during the Late (L) periods of both events. The two periods of stable magnetic field, M and L, bracket the Interim (I) period, in which the IMF exhibits dramatic alterations and the cross-field transport of protons dominates (panels (c) and (e) of both figures).

In the quiet magnetic environment of Period M, the proton transport proceeds predominantly along the magnetic field lines, but a special feature of the 2003 October 28 event is the arrival of the GLE proton flux from the southern directions of the antisolar hemisphere (Figure 3(d)), not from the solar hemisphere, as normally expected. In the 2001 April 15 event, Period L corresponds to the passage of the ICME, so the magnetic field is nearly perpendicular to the radial, Sun–Earth direction ($\lambda \approx -90°$) and exceptionally quiet. In the 2003 October 28 event, the magnetic field of Period L oscillated around the radial direction ($\lambda = -180°$). The 2003 October 28 event was observed in the wake of the recent ICME, the trailing edge of which had passed the Earth ~ 1.5 hr before the start of the GLE (Miroshnichenko et al. 2005; Richardson & Cane 2010).

Periods L of the two GLEs are quite different and are beyond the scope of our present study.

As always observed in GLEs, both events under study start with a kind of PC, the spectrum of which becomes steeper at high rigidities (the spectral parameter $\delta\gamma > 0$) and the angular distribution is anisotropic: the $\delta\gamma$ and $\langle \cos\theta \rangle$ profiles in panels (f) of Figures 2 and 3. However, the anisotropy of GLE 65 is almost twice that of GLE 60, indicative of a quantitative difference in the interplanetary transport parameters near the Earth orbit. The proton density profiles, N, in the panels (g) of both figures reveal both the main peak in the period M and the second, gentle peak in the period I, associated with proton transport across the magnetic field lines. The cumulative flux of energy up to a current time, $Q(t)$, is also plotted in panels (g). About 60% of the energy comes in the GLE's main phase (Period M), which is the focus of our present study.

The two GLEs are further compared in Figure 4, panels (a) and (b). The rise profiles of the proton flux, $S(t)$, up to and including the maximum in the two GLEs are almost identical (panel (a)). The shapes of the main phase decay are similar, but GLE 60 (the orange graph) decays nearly two times faster than GLE 65 (the blue graph). As an illustration of this relationship, we introduce a time transformation that stretches the GLE 60 decay by a factor of 2.2: $t' = t_M + (t - t_M) \times 2.2$ at $t > t_M$ and $t' = t$ otherwise. The flux profile of GLE 60 as a function of the modified time, $S(t(t'))$, is shown in Figure 4(a) with the red dashed line. After such a time transformation, the S-profiles of both GLEs nearly coincide, except for the late-phase decay at $t > 155$ minutes. The two GLEs diverge in Period L due to a difference in the strength of their DCs. The time profiles of the spectral index at 1 GV are mostly identical (the $\gamma/10$ graphs in Figure 4(b)), while the spectrum-steepening parameter $\delta\gamma$ in GLE 65 decreases twice faster than in GLE 60. The latter is illustrated with the time transformation $t'' = t_X + (t - t_X) \times 2$ applied to the GLE 65 profile, where $t_X = 10$ minutes is the X-ray flare maximum time. The stretched profile $\delta\gamma(t(t''))$ of GLE 65 is shown with the blue dotted line. It coincides with $\delta\gamma(t)$ of GLE 60 at $t < 155$ minutes. For these reasons and in this sense, the main phases of the two GLEs observed in Period M are similar.

4. Comparison with Data of Solar Electromagnetic Observations

Both selected events were associated with exceptionally strong ($>$X10) flares that had different durations and occurred in different complexes of ARs at different heliographic locations. The major solar eruption of 2003 October 28, with an X17.2/4B X-ray/optical flare at S16E08, was comprehensively observed (the eruption synopsis is compiled by Aurass et al. 2006). The flare of 2001 April 15 is only slightly weaker —its magnitude is X14.4/2B—located at S20W85 (e.g., Mészárosová et al. 2006, with a focus on the decimeter–radio and hard X-ray emissions). In panel (d) of Figure 4, we plot the soft X-ray profiles of both flares, with a reference time chosen so that both X-ray profiles reach their maximum values at the same time, $t = t_X = 10$ minutes. It is significant that with such a choice of the reference time, the proton flux profiles also reach their maximum values simultaneously at $t = t_M = t_X + (43 \pm 3)$ minutes (Figure 4(a)).

A soft X-ray image of the large-scale structure of the 2003 October 28 event is shown in Figure 4(h). The AR complex consisted of the six ARs (outlined by rectangles). The major
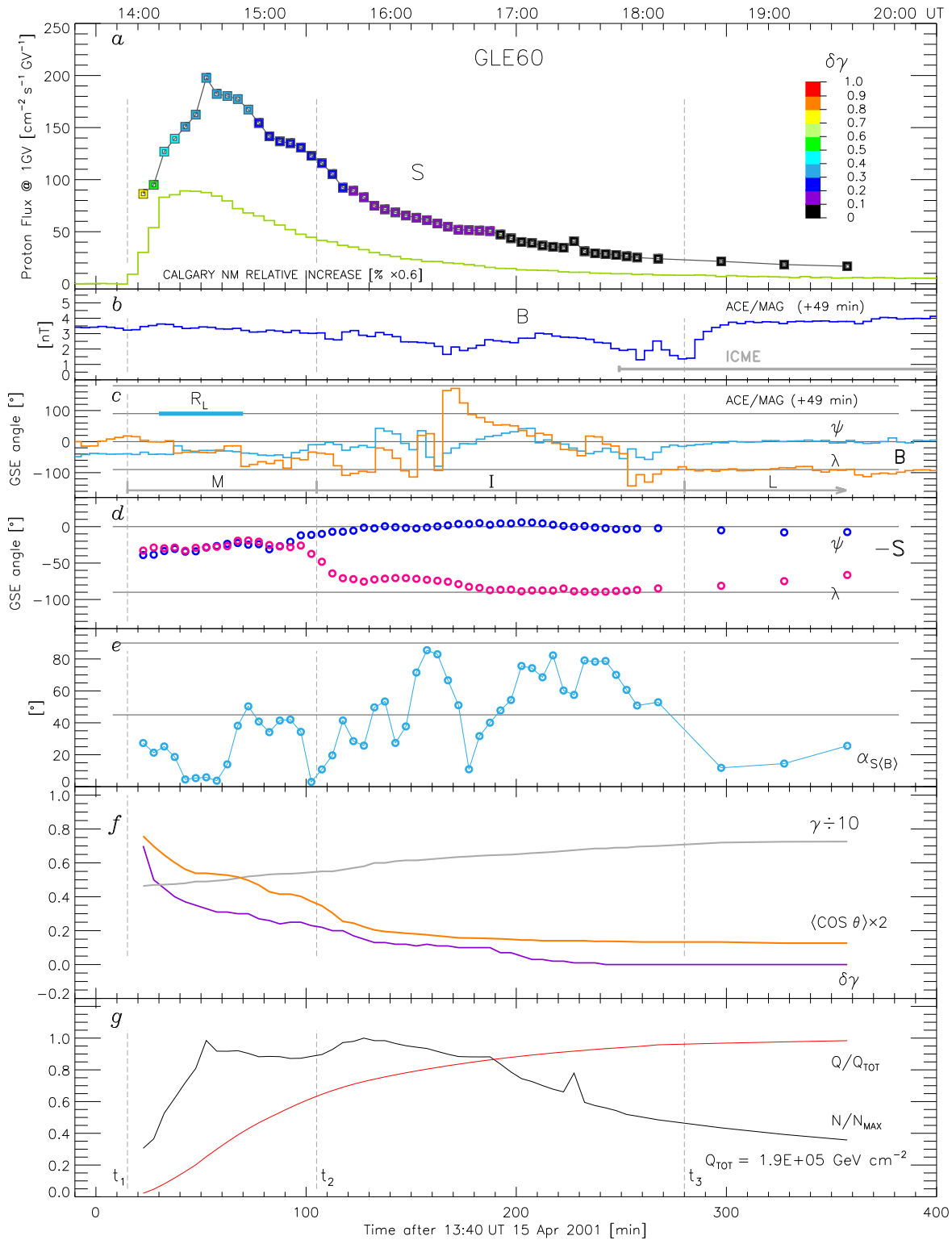
Figure 2. Overview of GLE 60. (a) Net flux of the GLE-producing solar protons, *S*, with the proton spectrum evolution illustrated with the point colors. Additionally shown is a sample of the NM count-rate profile. (b) The IMF magnitude *B* (4 minutes data by ACE/MAG). The ICME is according to Richardson & Cane (2010). The magnetic field timing is shifted for the solar wind transit time from the ACE orbit to the orbit of the Earth (49 minutes, at the solar wind speed $U = 480$ km s^{-1}). (c) The GSE angles, latitude ψ and longitude λ, of the IMF direction; the blue bar illustrates the timescale corresponding to the Larmor radius of 1 GV proton, $R_{\rm L}/U$. The three phases of GLE and the three sectors/streams of the solar wind in which these GLE phases were observed are denoted by the letters M (main), I (interim), and L (late). (d) The GSE angles of the direction from which the proton flux arrives, $-S$. (e) The angle $\alpha_{S\langle B\rangle}$ between the direction of the proton flux and the eight minute average magnetic line direction that is the closest to the direction of the proton flux regardless of the polarity of the IMF. (f) Proton spectrum parameters, $\gamma/10$ and $\delta\gamma$, and the average pitch-angle cosine of arriving protons, $\langle\cos(\theta)\rangle$. (g) The number density of 1 GV protons, *N*, and the cumulative energy fluence of the >1 GV protons, $Q(t)$. Its value at the end of the analyzed period of 485 minutes, $Q_{\rm TOT}$, is given in the panel.
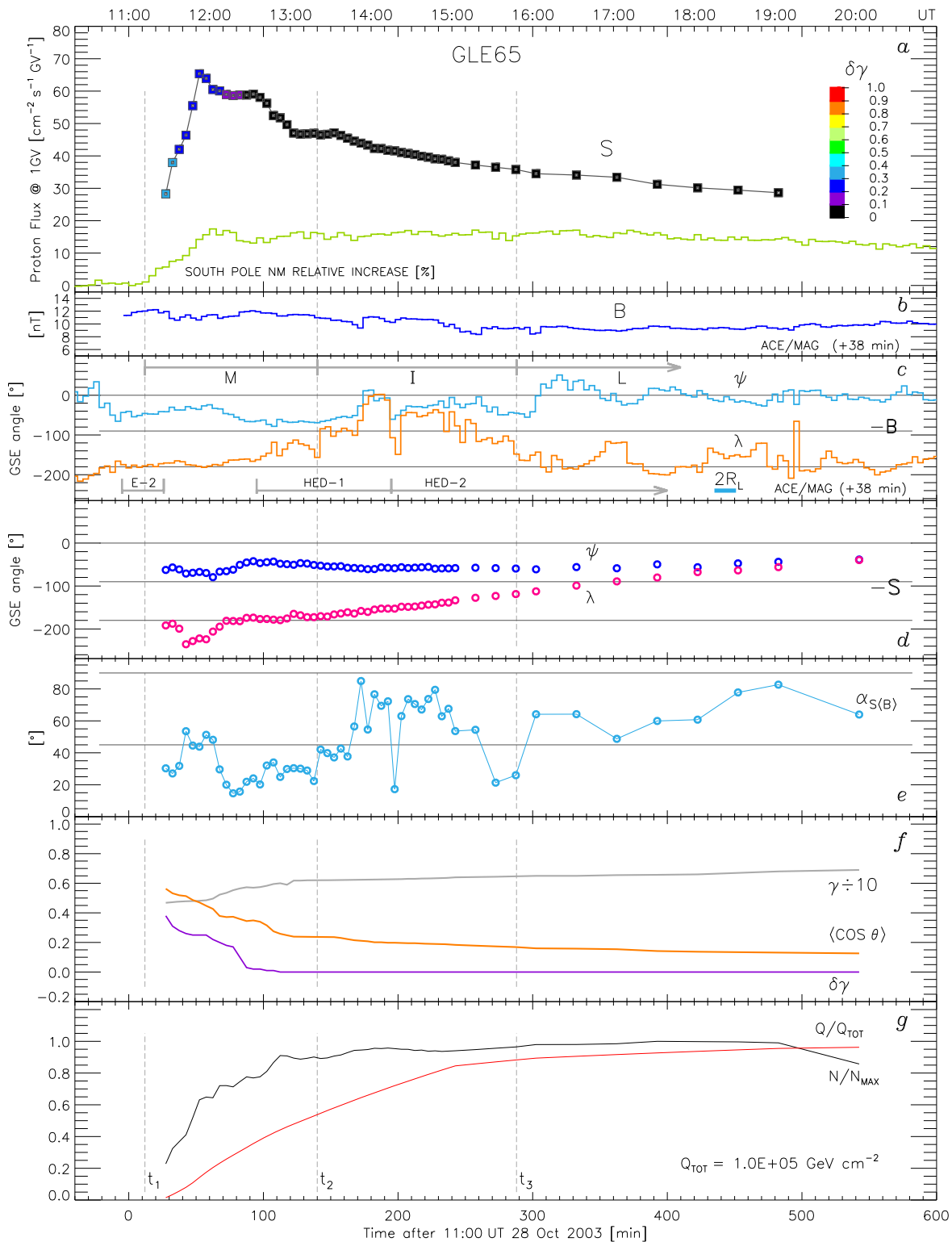
Figure 3. Overview of GLE 65: similar to Figure 2. Additionally indicated in panel (c) are the magnetic tubes E-2, HED-1, and HED-2, identified with solar energetic electrons, protons, and helium observed on Wind and SoHO. An impulsive electron event was observed in the magnetic tube E-2 when that tube reached the Wind spacecraft, which in 2003 was orbiting in the solar wind downstream of the Earth about the Lagrange point L_2 (the interval E-2 corresponds to the 27–182 keV electron rise in the instrument; Klassen et al. 2005). The deka-MeV nucleon^{-1} ion event was observed by ERNE in the magnetic tubes HED-1 and HED-2 (Figure 6(b)), when those tubes met SoHO near the Lagrange point L_1. The adopted solar wind transit time is: from SoHO to Earth 40, minutes; from ACE to Earth, 38 minutes; and from Earth to Wind, 24 minutes. The timescale corresponding to the double Larmor radius of a 1 GV proton is shown for the solar wind speed $U = 650$ km s^{-1}. The energy fluence, Q_{TOT}, is accumulated during the first 1025 minutes of the event.

optical flare was observed starting at $\approx$10 UT in the southern, large, and complex AR 10486. It was preceded by several subflares in that AR and in AR 10488 near the solar equator.

Simultaneously with the 4B flare in AR 10486, a subflare was observed in the small AR 10491 situated between the two big ARs (Solar-Geophysical Data, nos. 711 and 712, part 1, 2003;
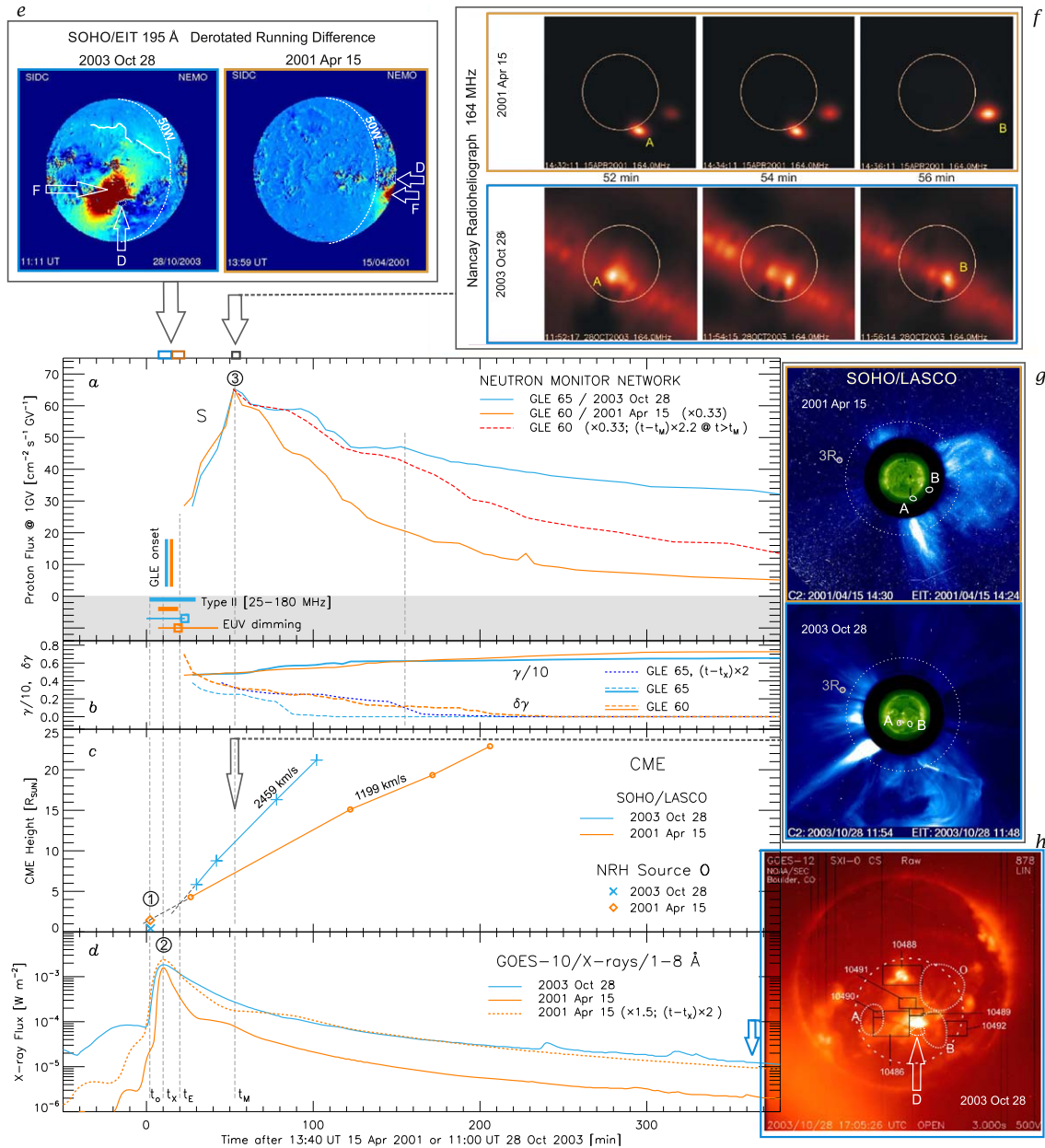
Figure 4. Comparison of the two GLEs and their progenitor solar eruptions. (a) Proton flux profiles of GLE 60 and GLE 65 ($S(t)$; solid curves). The dashed curve is for the decay profile of GLE 60 with time stretched by a factor of 2.2. At the bottom of the panel, thick horizontal bars indicate the timing of the radio type II bursts observed in the metric band at different observatories (SGD682, SGD712). The thin bars with square points show the time intervals of the coronal dimming (bars) and the peak times of the dimming area (points) measured from the 195 Å fixed-difference images by SoHO/EIT (according to the NEMO catalog; Podladchikova & Berghmans 2005). Note: a scatter-free transport time of GLE protons from the Sun to the Earth along the standard IMF line exceeds the flight time of light by ≈2.5 minutes, not accounted for in plotting. (b) Spectral parameters of the GLE-producing solar protons, $\gamma/10$ and $\delta\gamma$. The blue dotted curve is the $\delta\gamma$ profile of GLE 65 with the time stretched by a factor of 2. (c) Time–height profiles of the LASCO CMEs. As an early signature of the eruption onset, we show the first new radio source observed at 164 MHz by NRH (Sources O in Figure 5; label ①). (d) Soft X-ray profiles of the two flares (solid curves). The reference times are chosen so that the flare peaks coincide (label ②). The dotted curve refers to 2001 April 15, with time uniformly stretched by a factor of 2 on both sides of the intensity peak. The four points in time common to both events are: t_o—the first signature in 164 MHz of the eruption beginning; t_X—the maximum of the soft X-ray flare; t_E—the maximum of the EUV dimming area; and t_M—the proton flux maximum. (e) Derotated running difference images in 195 Å at around the GLE onset time. The images are created with the NEMO software package using the SoHO/EIT frames acquired at a 12 minutes cadence, in a color scale that shows brightenings with colors from cyan to red, and dimmings in blue. The strongest EUV dimming area deduced from the derotated fixed different images is outlined with the small dotted contour shown with Arrow D in each frame (in the case of the 2003 October 28 event, there is a comprehensive description of the EUV dimming by Podladchikova & Berghmans 2005). Arrow F points to the center of the major optical flare. The white curve in the left frame marks the leading edge of the global coronal wave (EUV wave) as identified by Muhr et al. (2010). (f) Successive flashes of two radio sources, A and B, observed at around the GLE peak time in both events (NRHat 164 MHz). (g) The LASCO/C2 images at the GLE peak time. Overlaid on the CME images are the radio sources A and B from panel (f). Source A is located near the boundary between the expanding CME and the neighboring helmet streamer. (h) Soft X-ray image of the Sun in the decay phase of the 2003 October 28 flare (17:05 UT; GOES-12/SXI data). The black rectangles bound the flaring AR 10486 and the five surrounding ARs (the sunspot groups observed at the Holloman Solar Observatory at 17:14 UT; SGD712). The dotted ovals outline the 164 MHz radio sources: the first new source, which emerged at 11:02 UT (Source O in Figure 5), and the S-peak-associated Sources A and B from panel (f). Arrow D points at the strongest EUV dimming area, the same as in panel (e), but corrected for the solar rotation. The possible location of the relativistic proton source (Source q_0) is bounded by the dashed circle that includes the coronal locations of the radio sources O, A, and B, because such sources are similarly associated with the production of both GLEs (the EUV wave location shown in panel (e) is not included for the reasons explained in Section 6.3).
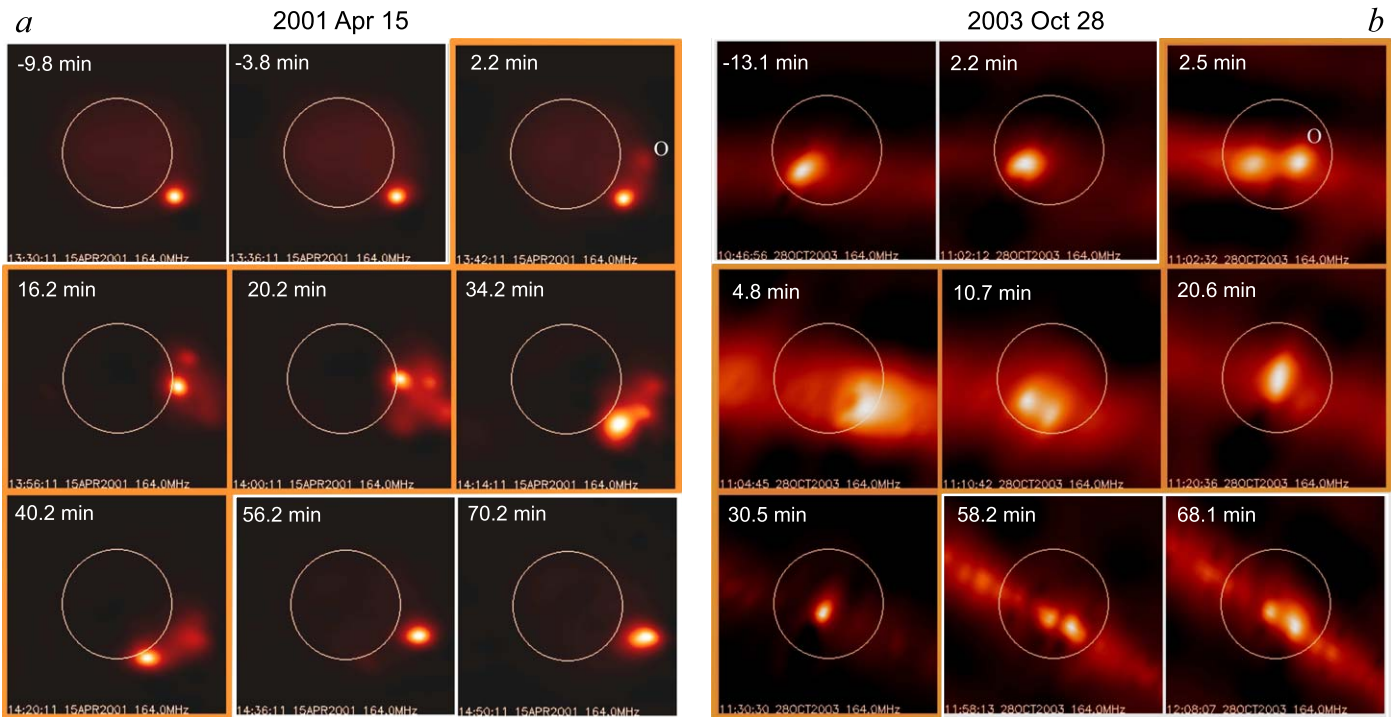
Figure 5. Transient radio sources associated with the rise phase of GLE 60 and GLE 65 (snapshots in orange frames). The images were taken by the NRH in 164 MHz (https://secchirh.obspm.fr/) at the relative times indicated on the frames (the reference times are 13:40 UT on 2001 April 15 and 11:00 UT on 2003 October 28). The first emerged source of an eruption is labeled O. The first two frames and the last two frames in each event show the stationary sources before and after the eruption.

hereafter, SGD711 and SGD712, respectively). The 2001 April 15 complex also consists of six ARs—the flaring AR 9415, surrounded by AR 9420, AR 9424, AR 9427, AR 9417, and AR 9425 (Solar-Geophysical Data, nos. 681 and 682, part 1, 2001; hereafter, SGD681 and SGD682, respectively). The two latter ARs were hidden behind the west limb from April 14, so we do not illustrate the AR complex of 2001 April 15. The soft X-ray flare on 2003 October 28 was twice as long as the flare on 2001 April 15, which is illustrated in Figure 4(d) by a twofold stretching of the latter flare profile on both sides of its maximum, with the time transformation $t'' = t_X + (t - t_X) \times 2$ (dotted curve).

The impulsive phase of the 2003 October 28 flare in metric radio emissions started with pulsations at 11:01 UT (Aurass et al. 2006, Table 2 therein). In the 164 MHz images by the NRH, this corresponds to the appearance at 11:02 UT on the solar disk of a new source located northwest of the flaring AR 10486, while previously the emission was dominated by a stable source located northeast of AR 10486 (the first new source is marked O in Figure 5(b) and in panel (h) of Figure 4, and can also be seen in Figure 3 of Miroshnichenko et al. 2005). In that on-disk flare, the Moreton wave was well observed (in Hα filtergrams by the Meudon observatory; Muhr et al. 2010). The extrapolated start time of the Moreton wave was at 11:01 UT (Figures 8 and 9 of Muhr et al. 2010). The Moreton wave start immediately preceded the beginning of the hard X-ray burst/the flare's impulsive phase and the emergence in 164 MHz of Source O. For this reason, the start time of Source O can serve as a benchmark for the entire eruption. In the case of the 2001 April 15 flare, the first new 164 MHz source, Source O, appeared at 13:42 UT north of the previous stable source, both located at $\sim 0.4 R_\odot$ above the solar west limb (Figure 5(a)). The first radio sources of both events are shown

in Figure 4(c) with the two points at $t = t_o = 2$ minutes (label ①).

The Moreton wave on 2003 October 28 swept across the solar disk during 11:02 UT–11:13 UT (Muhr et al. 2010). Its coronal counterpart, the global coronal EUV wave (the EIT wave), is evident in the EUV images by SoHO/EIT. However, the EUV waves are observed with much lower cadence compared to the optical observations. Two frames of Figure 4(e) show the global coronal waves at around the onset time of GLE 60 and GLE 65. In both cases, the GLE onset was observed when the EUV wave was passing through the western longitudes $\sim$ W50°. Concurrently with the coronal waves, EIT observed the coronal dimmings, indicative of a decrease in the coronal plasma density caused by a CME (Thompson et al. 1998). Arrow D in both frames of Figure 4(e) points at the strongest dimming area situated near the flaring AR (the flare location is shown with the F arrow). The time intervals of the observed EUV dimmings are indicated in panel (a). In both events, the dimming area reached its maximum value at $t \approx t_E = 20$ minutes. The GLE onset occurred during the coronal dimming, 5–10 minutes before the peak of the dimming area.

The GLE onsets were also associated with the metric type II bursts, a signature of coronal shocks. On 2003 October 28, a type II burst at 180 MHz started at around 11:02 UT (SGD712; Klassen et al. 2005; Muhr et al. 2010). On 2001 April 15, a type II burst at 180 MHz began at 13:47 UT (SGD682). The timings of the metric type II bursts are indicated in panel (a) of Figure 4. Both GLEs began to rise when the metric type II bursts were in progress, and continued to rise well after the passage of the global coronal waves and after the end of the metric type II bursts.

The LASCO CME images at the peak time of the proton flux S are shown in Figure 4(g). In both events, a CME-plus-
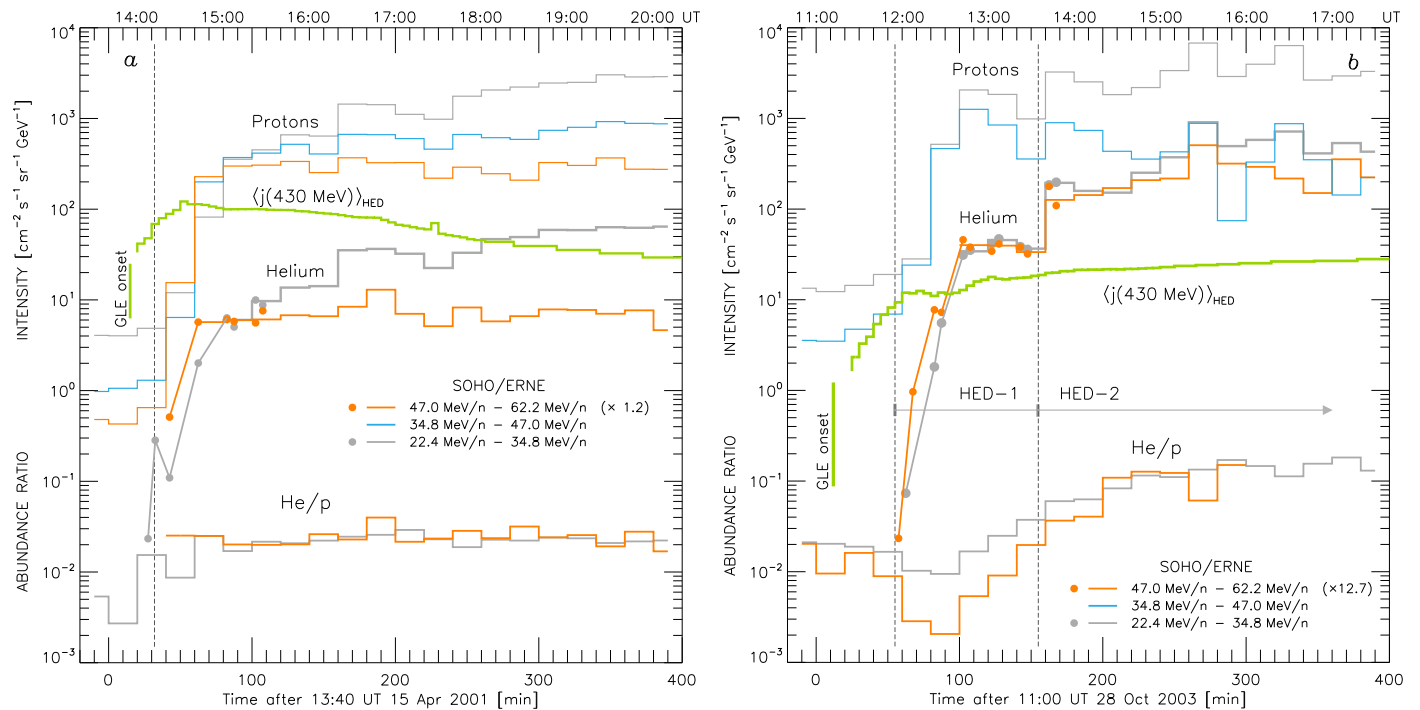
Figure 6. Time–intensity profiles of the proton and helium intensities in three energy channels of SoHO/ERNE and in the virtual 430 MeV proton channel inferred from the NM data, for the events of 2001 April 15 (a) and 2003 October 28 (b). The points are for the 5 minutes data, with data gaps between some of them. The ERNE event onset is shown with the vertical dashed line. Also shown are the helium abundance profiles, He/p. In the case of the 2003 October 28 event, we can distinguish the two time intervals/IMF tubes—HED-1 and HED-2—populated with SEPs produced by the two different sources—the helium-poor source q_1 and the helium-rich source q_2. The helium abundance change at around 13:35 UT was caused by the entry of the spacecraft into the magnetic tube already containing the helium-rich SEPs, and not by the fresh injection of the helium-rich composition from the Sun, since the anisotropy of the proton flux did not increase, as might be expected with a fresh injection, but decreased (Figure 7). The identified intervals HED-1 and HED-2 are compared with the IMF data in Figure 3(c).

streamer structure is observed. However, the heliographic locations of the AR complexes at the CME base and, accordingly, the CME orientations are different. The CMEs differ significantly both in the CME speed observed by LASCO at the heliocentric distances $>3R_\odot$, 1199 km s^{-1} versus 2459 km s^{-1}, and in the CME height at the time of the maximum proton flux ($t = t_M$), $7.4R_\odot$ versus $11.1R_\odot$, at position angles 268° and 15°, respectively, for 2001 April 15 and 2003 October 28.

The rise of the proton flux S proceeded concurrently with the irregular emergence of the 164 MHz sources at different locations, as observed by NRH and exemplified with the orange-framed snapshots in both panels of Figure 5. At around the S-peak time, the identically organized flashes of two radio sources, A and B, were observed in both events (Figure 4(f)). Souce A in both events was on the CME side next to the helmet streamer (Figure 4(g)) and was the closest in time to the peak of the proton flux. In four minutes after Source A, Source B flashed and Source A disappeared. Coronal radio sources became stable after 14:34 UT–14:36 UT on 2001 April 15 and after 11:56 UT–11:58 UT on 2003 October 28, i.e., at $t > 56$ minutes, when the proton flux of both GLEs declined.

A review of the solar radio data in the microwave band from the Astronomical Institute in Ondrejov has revealed no enhancement that could be associated with the proton flux maximum in either of the two events. We have also inspected the metric to dekametric and dekametric to hectometric radio spectrograms from the San Vito Solar Observatory and Wind/WAVES, respectively. In both events, the low-frequency type III bursts (type III-l by Cane et al. 2002) were observed before and close to the GLE onset. A series of the low-

frequency type III bursts persisted during the entire rise phase of the proton flux in the 2001 April 15 event, but no such series was observed on 2003 October 28 (see also Klassen et al. 2005, Figure 1 and Table 1 therein). The interplanetary type II bursts, from 14 MHz down to 40 kHz, were observed in both events. A low-frequency type II burst continued in the 2001 April 15 event for about 23 hr, starting at 14:05 UT, and in the 2003 October 28 event for about 37 hr, starting at 11:10 UT, well after the S-peak time, and there were no significant features at $t = t_M$. A strong hectometric type IV burst was observed on 2003 October 28 after 11:40 UT, but no type IV burst was observed on 2001 April 15.

5. Comparison with SoHO/ERNE Data

The HED of SoHO/ERNE has a 120° wide viewing cone with the axis pointing, in the events considered here, along the nominal Parker spiral, i.e., 45° west of the Earth–Sun direction in the plane of the ecliptic. Figure 6 shows the viewing-cone-integrated intensities of protons and helium in the three energy channels, 22.4–34.8 MeV nucleon^{-1}, 34.8–47 MeV nucleon^{-1}, and 47–62.2 MeV nucleon^{-1}. For a comparison of the NM data with the ERNE measurements, we have introduced a virtual ERNE channel that counts the NM-observed protons in the viewing cone of ERNE/HED, $\Delta\Omega_{HED}$:

$$\langle j(E, t)\rangle_{HED} = \frac{dP/dE}{\Delta\Omega_{HED}} \int_{\Delta\Omega_{HED}} j(P, \theta, t)d\Omega. \qquad (7)$$

The deduced 430 MeV proton profiles are shown in both panels of Figure 6.

Based on the helium-to-proton abundance ratio, SEP events can be divided into two categories: helium-rich events with He/p $\gtrsim 0.1$ and helium-poor events with He/p $\lesssim 0.01$ (Van Hollebeke 1975). The 2001 April 15 event was helium-poor, He/p ≈ 0.02. The 2003 October 28 event also started with a helium-poor composition, He/p $\lesssim 0.01$, in the time interval HED-1. Then, in the interval HED-2, it was replaced by a helium-rich composition, He/p ≈ 0.1. There was also a difference in the onset time of the deka-MeV event relative to the onset of the corresponding GLE event: the 2003 October 28 event started ≈ 25 minutes later than the 2001 April 25 event.

In the case of the 2003 October 28 event, also available are the ERNE measurements of the proton arrival directions. Figure 7 illustrates the anisotropy of the 17–22 MeV proton flux during the event. The time evolution of the proton flux anisotropy is illustrated in panel (a), with the proton intensities integrated over the five sectors of the ERNE/HED viewing cone that are defined in the insert. The corresponding anisotropy indices are introduced and plotted in panel (b). The two indices, $I_{\mathrm{NORTH-SOUTH}}$ and $I_{\mathrm{SUN-WEST}}$, characterize the north–south asymmetry and the east–west asymmetry of the proton intensity in the instrument's viewing cone. For comparison's sake, in panel (c), we plot similar indices for the GLE-producing protons arriving within a field of view equivalent to that of HED. The deka-MeV proton flux arrived from the northern hemisphere, while the GLE protons arrived from the southern directions (Figure 7, panel (b) versus panel (c); see also Figure 3(d)).

In the insert to panel (a), the white diamond shows the direction of the 17–22 MeV proton flux, estimated as the symmetry axis of the model angular distribution, a part of which was counted in the 241 small sectors of the HED's field of view. The deka-MeV proton flux is well aligned along the direction of the magnetic field shown by the red circle, but not so for the GLE proton flux (blue square), which made a 120° angle with the the flux of the deka-MeV protons. Note that the solar wind transit time from the SoHO orbit to the Earth on 2003 October 28 was 40 minutes. For this reason, the flux direction of the GLE-producing solar protons is shown for the correspondingly delayed time, in order to compare the particle fluxes observed in one and the same magnetic tube of the solar wind.

6. Discussion

6.1. Morphology of GLEs

The time profiles of GLEs shown in Figure 1 are very diverse. A well-separated, short PC, defined as an anisotropic flux of protons with a strongly steepening spectrum, is observed in the beginning of events like GLE 59 on 2000 July 14. In some other events, like GLE 72 (2017 September 10), a short PC in the beginning of the GLE is visible, but relatively weak. In GLE 72, the weak PC pulse is followed by a more prolonged emission of a similar, non-power-law spectrum. Such an emission will be referred to as an extended prompt component (EPC). The two events selected for the present investigation, GLE 60 and GLE 65, start with a kind of EPC emission, and here we focus on the nature of this component. The PC/EPC ejections are supplemented/followed by the emission of the DC, discussed elsewhere (in the case of GLE 72, see Kocharov et al. 2020, 2021).

6.2. Interplanetary Transport

The observed GLE profiles depend both on the proton injection at/near the Sun and on the transport in different IMF structures, as well as on the state of the Earth's magnetosphere. We have selected for this study two GLEs with similar proton parameters outside the magnetosphere, so only solar and interplanetary factors are left for consideration. The interplanetary transport depends on the state of the solar wind with its frozen-in magnetic field. The available measurements of the IMF are local, while the SEP transport depends on the IMF structures on the entire route from near the Sun to 1 a.u. The low-rigidity particles, such as electrons and nonrelativistic protons, follow the IMF lines more closely than relativistic protons, so they can provide additional information about the global structures inside and around the Earth's orbit.

Although the ability for cross-field transport increases for high-energy protons, especially at locations of irregular IMF, in general their longitudinal transport is limited and the observed GLE profiles depend on the position and size of the high-energy proton source on the Sun relative to the observation point. In contrast to lower energies, multipoint (stereoscopic) observations of a particular high-energy event are not available. For this reason, we have to rely on a rotational stereoscopy approach, in which the particle emission in a series of events produced by the same AR during its passage across the solar disk is assumed to be nearly the same in all events of the series. Figure 1 reveals that the GLEs of the 2003 October–November series (GLEs 65–67), associated with flares at longitudes from E08 to W56, do not differ from each other as much as the GLEs of the October 1989 series (GLEs 43–45, associated with flares at E10–W57). A possible explanation is that the short PC seen in GLE 44 is emitted in a much narrower range of solar longitudes compared to the EPC dominating the GLE 65–67 series. On such empirical grounds, the difference in the heliographic location of the progenitor eruptions of GLE 60 and GLE 65, W85 versus E08, is not dramatic in terms of the GLE shape, because both GLEs are dominated by the EPC.

In the main phase of both GLE 60 and GLE 65 (Phase M in Figures 2 and 3), the high-energy solar protons arrived mainly along the IMF lines (panels (e) of both figures). Three populations of energetic electrons were identified by Klassen et al. (2005) during the duration of the 2003 October 28 event; here, we designate the electrons in periods I, II, and III of their Figure 1 as E-1, E-2, and E-3, respectively. The closest to the GLE 65 onset was the component E-2, a highly anisotropic, impulsive electron component, registered below 0.182 MeV on the Wind spacecraft, arriving from the Sun in the magnetic tube labeled E-2 in Figure 3(c). Miroshnichenko et al. (2005) attributed those subrelativistic electrons to an acceleration in the western solar hemisphere, where one of the radio sources was located and from where the electrons could arrive along a Parker-type magnetic field line. However, the GLE protons in that event unexpectedly arrived from the antisolar hemisphere (Figure 3(d)). The arrival of protons in the 2003 October event from the antisolar direction was previously explained by the proton transport along the hypothetical IMF loop rooted near AR 10486 (Miroshnichenko et al. 2005, Figure 9 therein).

On October 28, the ICME passed the Earth during 02:30 UT–09:00 UT. By the GLE onset at ≈ 11:10 UT, the trailing front of the ICME was already behind the Earth at a distance of about 0.03 a.u. We observe an enhanced cross-field transport of protons in the strongly disturbed magnetic field of Period I
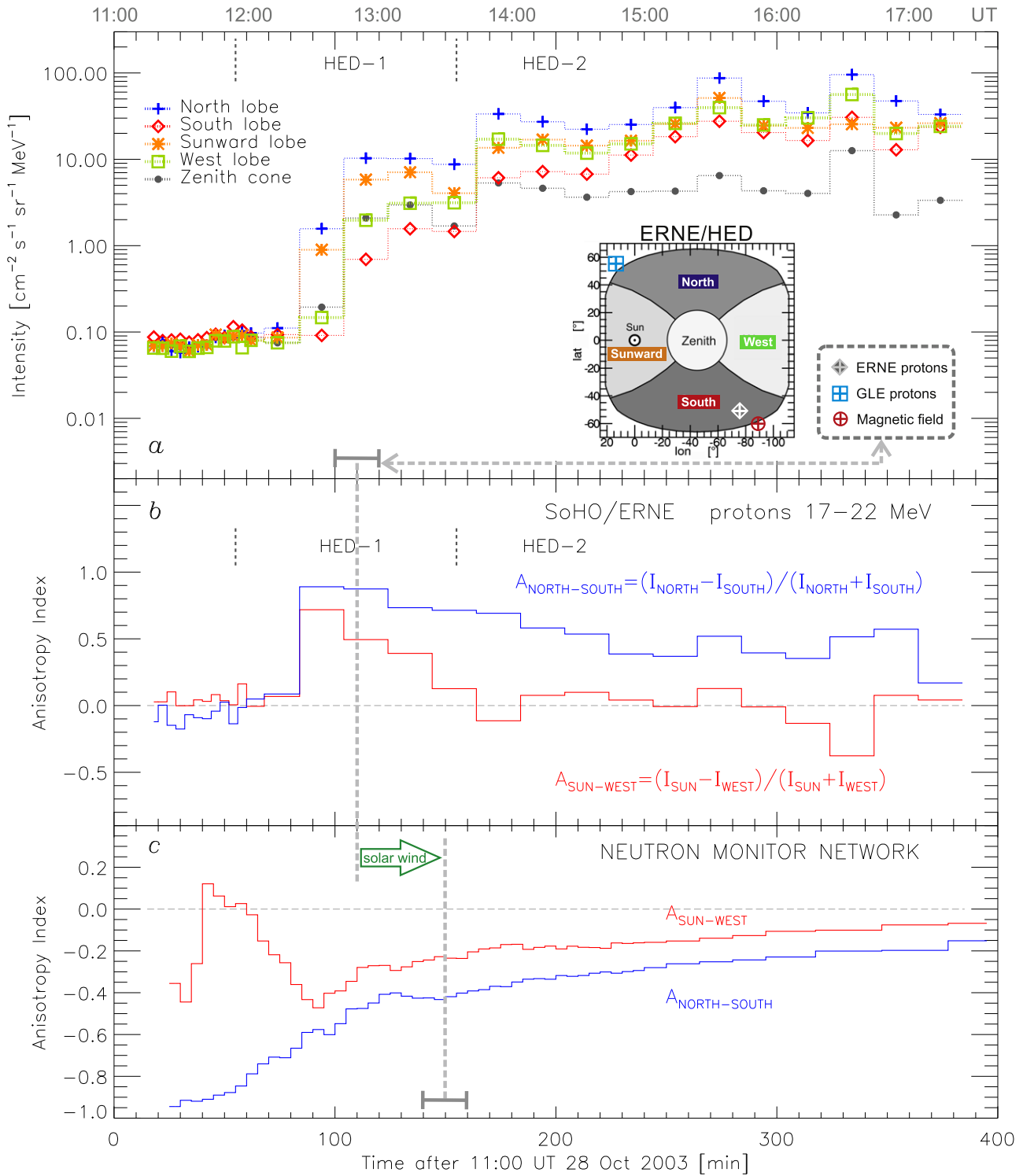
Figure 7. Comparison of the proton flux anisotropy observed on 2003 October 28 in the deka-MeV range by the HED of the ERNE instrument on board SoHO and in the GV range by the NM network on the Earth. (a) Time profiles of the 17–22 MeV proton intensities in the five large sectors of the HED's field of view. The insert shows the field of view of ERNE/HED divided into the five sectors over which the proton intensities are integrated (GSE longitude and latitude). The points in the insert additionally show three directions: (1) the white diamond indicates the flux direction of the 17–22 MeV protons estimated using the proton registration in 241 small sectors of HED during 12:40 UT–13:00 UT, so the protons flow from northeast to southwest; (2) the blue square shows the flux direction of relativistic protons deduced from the NM data at 13:20 UT–13:40 UT; and (3) the red circle shows the direction opposite to the direction of the IMF ($-B$) at 12:44 UT–13:04 UT (average of 4 minutes ACE/MAG data). The time periods HED-1 and HED-2 are the same as in Figure 6(b). (b) Two anisotropy indices, $A_{\mathrm{NORTH-SOUTH}}$ and $A_{\mathrm{SUN-WEST}}$, which are defined in the panel and use the sectorial intensities plotted in panel (a). (c) Similar anisotropy indices for the GLE-producing protons. The green arrow illustrates the time it takes for the magnetic tube to travel from SoHO to the Earth's orbit, so a 40 minutes shift is applied when comparing in the insert of panel (a) the proton flux directions measured at two different locations.

(Figures 2 and 3). The ICME also strongly disturbs the IMF around it, and so could enhance the cross-field transport of the GLE protons. If there were no IMF loop directly connecting the

relativistic proton source on the solar disk to the Earth, the protons could reach the Earth-connected IMF lines by decoupling from the IMF lines and cross-field transport in

the magnetic field draping near the ICME behind the Earth, and then return to the Earth from the antisolar hemisphere. The ICME-enhanced cross-field transport of the GLE 65 protons and the large size of the EPC sources on the Sun may explain why the $\approx 93°$ difference in heliographic locations of the flares associated with GLEs 60 and 65 did not cause differences in their shapes.

In the 2003 October 28 event, SoHO/ERNE detected in the deka-MeV nucleon^{-1} range both a helium-poor particle flux and a helium-rich flux. The initial, helium-poor phase of the event was observed in the period/magnetic tube HED-1 (Figure 6(b)). Tube HED-1 partly coincided with the interim solar wind stream of Period I (Figure 3(c)), in which the magnetic field was strongly disturbed and the GLE protons and the ERNE-registered protons arrived from different directions (the insert to panel (a) of Figure 7). We suggest that three proton and helium sources, which we will call q_0 to q_2, contributed to this SEP event. The GLE protons from Source q_0 reached the magnetic tube HED-1 largely via the cross-field transport, while the deka-MeV protons of the helium-poor component arrived along the IMF lines from a very different direction and from an another source, Source q_1. Concurrently with the arrival of the ERNE-registered protons, the Comprehensive Suprathermal and Energetic Particle Analyzer, also on board SoHO, observed a gradual increase of relativistic electrons, the electron component E-3 (Klassen et al. 2005), apparently from the same, magnetically connected Source q_1. Source q_1 may be identified with the CME bow shock in the solar wind. The gradual electron component E-3 differed from the previous, impulsive electron component E-2. The E-2 emission may be associated with the passage of the EUV wave at western solar longitudes during 11:08 UT–11:17 UT (Figure 1 by Klassen et al. 2005, their time interval II plus 8 minutes versus our Figure 4(e)).

One more source, Source q_2, is required to produce the helium-rich component of the deka-MeV nucleon^{-1} ions. At the transition from the helium-poor period HED-1 to the helium-rich period HED-2, the ion intensities increased, while the proton flux anisotropy decreased (Figures 6 and 7). This is not what would be expected in the case of a new, fresh injection of helium-rich SEPs. If so, then the observed change in the composition and energy spectrum of SEPs should be explained by the entrance of the spacecraft into the magnetic tube HED-2, which was already filled with SEPs from a helium-rich Source q_2. The transition from HED-1 to HED-2 was accompanied by an abrupt rotation of the IMF (Figure 3(c)).

The strongly disturbed solar wind of Period I (Figures 2(c) and 3(c)) comprises several entangled magnetic tubes whose directions differ from each other by $\sim 90°$. The helium abundance variations observed in the 2003 October 28 event suggest the IMF tubes were connected to different sources of the deka-MeV nucleon^{-1} ions situated at different heliographic locations. The transport of high-energy protons in such a magnetic structure proceeds mainly across the magnetic field, and due to this, the high-energy protons from Source q_0 filled all the tubes. The traditional assumption of the field-aligned propagation of high-energy protons is not valid everywhere, and the corresponding cross-field transport models are under development (e.g., Marsh et al. 2013; Laitinen & Dalla 2017).

6.3. Solar Origins of GLEs

Both GLE 60 and GLE 65 were associated with an exceptionally strong flare and a fast and wide CME that interacted with a nearby streamer (Figure 4(g)). However, the CMEs differed dramatically in the magnitude of the CME speed in the LASCO field of view, by a factor of 2.05 (Figure 4(c)). The CME heights at the moment of maximum proton flux differed by a factor of 1.5: $7.4R_\odot$ versus $11.1R_\odot$. Hence, the CME expansion at heliocentric distances $>3R_\odot$ is unlikely to account for why GLEs 60 and 65 are similar. It is also unlikely that CME expansion far from the Sun could cause the sharp peak in the proton flux at t_M without corresponding signatures in the low-frequency radio emissions, but with a similar flashing of the radio sources A and B far behind the CME (Figure 4(f)).

Torsti et al. (1999) reported for a deka-MeV proton event associated with a flare at S30E15 that the proton injection at the roots of the Earth-connected IMF lines started upon the arrival at the western longitudes of the global coronal wave observed by SoHO/EIT (for more observations of this kind and discussion, see Park et al. 2013 and references therein). A fraction of impulsive electron events can also be associated with the propagation of EUV waves, rather than the flare itself (Krucker et al. 1999). The onsets of both GLEs under present study were observed when the corresponding EUV wave had arrived at $\approx W50°$ (Figure 4(e)). In the 2001 April 15 event, the first deka-MeV nucleon^{-1} protons and helium arrived 20–30 minutes after the relativistic protons (Figure 6(a)), as expected based on their different transit times from the Sun. However, in case of the 2003 October 28 event, there were no corresponding deka-MeV protons or helium registered with SoHO/ERNE above the actual background (Figure 6(b)), while the deka-keV electrons did arrive (Klassen et al. 2005, their second impulsive component is designated by us as E-2). The idea that the first high-energy protons on 2003 October 28 were emitted by the global coronal shock upon its arrival at $\sim W50°$ contradicts the observational data, because in such a case, both the GLE-producing protons and the energetic electrons would have arrived along the magnetic field lines from the solar direction, whereas the GLE-producing protons had arrived from a very different direction (Figure 7), and obviously from a different source. Alternatively, there may be no causal relationship between the EUV wave arrival at W50° and the high-energy proton emission, and the wave arrival at W50° just happens to have occurred when the relativistic protons were emitted from a different part of the same eruption. Concurrently with the global coronal waves, the EUV dimming areas are typically observed (Podladchikova & Berghmans 2005), so the EUV dimmings can always be an alternative association. In the 2003 October 28 event, the EUV wave is the most likely source of the electron component E-2, while the GLE protons arrived from a distinct source, Source q_0, which alternatively should be associated with coronal dimming.

In each of the two eruptions, the soft X-ray flare reached its maximum in 8 minutes after the emergence of the first new 164 MHz source (point ② versus point ① in Figure 4). The emergence of the metric radio sources and their fast evolutions continued in both events until the time $t \approx 56$ minutes (Figures 5 and 4(f); the corresponding label ③ in Figure 4(a)), which indicated dynamic changes in the large-scale structures of the coronal magnetic field above the AR complex. The matches ①–②–③ mean for us a similarity of the

near-Sun eruption development and post-CME evolution. In both selected events, the relativistic proton flux reached its maximum value in 43 minutes after the maximum of the soft X-ray flare, at $t = t_M = 53$ minutes, shortly before the end of the period of the dynamic changes of the magnetic field over the AR complex. After the end of the post-CME reconfiguration and magnetic field closing, the proton escape into the solar wind declined. The rise and peak profiles of both GLEs coincide (Figure 4(a)). A straightforward interpretation is that the similarity of the two GLEs is caused by a similar eruption development over their AR complexes after the flare pulse and the CME departure. Based on the set of exact timing matches and the observed radio source locations, the locus of the base of the relativistic proton source is estimated to be within $\approx 0.5 R_\odot$ around the solar flare site (the dashed circle in Figure 4(h)).

The two X-ray flares were almost of the same magnitude, but differed significantly in their duration—the 2001 April 15 flare decayed twice as fast as the flare on 2003 October 28. We find a similar relation between the rates of the proton flux decay in the main phase of the GLEs (Figure 4(a) at $t < 155$ minutes). The timescales of the soft X-ray flare decay and the GLE decay of 2003 October 28 were longer than the corresponding timescales of the 2001 April 15 event by the factors of $\tau_X^{(65)}/\tau_X^{(60)} = 2$ and $\tau_{GLE}^{(65)}/\tau_{GLE}^{(60)} = 2.2$, respectively. The decrease in time of the spectral parameter $\delta\gamma$, which describes the rate of spectrum steepening with rigidity and the corresponding progression of the power-law spectrum toward higher rigidities, in GLE 65 proceeded twice as fast as in GLE 60: $\tau_{\delta\gamma}^{(60)}/\tau_{\delta\gamma}^{(65)} = 2$ (Figure 4(b)). The LASCO CME speeds related as $V_{CME}^{(65)}/V_{CME}^{(60)} = 2.05$. All four ratios agree with the 10% accuracy:

$$\frac{\tau_{GLE}^{(65)}}{\tau_{GLE}^{(60)}} = \frac{\tau_{\delta\gamma}^{(60)}}{\tau_{\delta\gamma}^{(65)}} = \frac{V_{CME}^{(65)}}{V_{CME}^{(60)}} = \frac{\tau_X^{(65)}}{\tau_X^{(60)}} = \Re, \qquad (8)$$

where the eruption "strength" factor $\Re = 2$–2.2. Note that it is equal to the ratio of the timescales of the major soft X-ray rises (Figure 4(d)) that preceded the post-impulsive-phase phenomena of Equation (8).

With a general, large sample of the solar eruptions, Kahler & Ling (2022) found a correlation between the CME speed and the X-ray flare decay time. Our present observation of the two eruptions is consistent with that general pattern; even a perfect proportionality is present. A slow decay of the flare's soft X-ray emission, on timescale of hours, implies the existence of extended heating on the same timescale, e.g., by the slow dissipation of turbulent Alfvén waves (Ashfield & Longcope 2023) after the CME departure. On the other hand, turbulence left behind the CME in coronal structures adjacent to the X-ray-emitting loops could (re)accelerate protons and thereby change the total number of 1 GV protons ($S(1\,GV)$) and the spectrum shape ($\delta\gamma$), which may explain the correlation between the GLE decay time and the X-ray flare duration. The turbulence level left behind the CME should be proportional to the CME speed. However, no theoretical models of this kind yet exist.

Klein et al. (2001), based on a detailed analysis of GLE 59 on 2000 July 14, concluded that the observations support the idea that the relativistic protons (of the PC) were accelerated during the reconfiguration of the coronal magnetic fields, at heights between 0.1 and $1\,R_\odot$ above the photosphere, and not in the flaring AR or at the bow shock of the CME. An overview of that event is shown in Figure 8. The GLE rise profile was found to be similar to the time profile of the metric continuum sources situated west of the flaring AR 9077 (Klein et al. 2001, Figure 5 therein). Those radio sources are shown in their Figure 7(a) and, based on it, in the insert to our Figure 8. The radio source progression to lower frequencies (higher altitudes) is illustrated with successive snapshots at the fixed frequencies shown with the color contours in the insert to Figure 8, along with the trajectory of the EUV filament ejected from AR 9077. The observed frequency dispersion of the metric continuum sources (a higher-frequency emission rose earlier and reached its maximum earlier than a low-frequency emission) and the well-defined low-frequency cutoff imply that the radiating electrons were confined within a closed large-scale magnetic structure connecting the leading part of AR 9077 with regions of weak magnetic field in the western hemisphere (Klein et al. 2001).

Similar to other events with a short PC (GLE 64 and GLE 70), the PC pulse of GLE 59 occurred concurrently and reached its maximum value simultaneously with the EUV dimming area observed by SoHO/EIT (Figure 8). The EUV dimming regions are caused by evacuation of the coronal plasma in the course of the magnetic flux rope ejections and the driven magnetic reconnection of ambient coronal structures (Attrill et al. 2006 and references therein). The latter leaves imprints in metric radio emissions like the moving continuum shown in the insert to Figure 8 and the radio bursts of type III-l emphasized by Cane et al. (2002). The rise of GLE 59 was correlated well with both the rising sources of the metric emissions and the EUV dimming left behind.

The CME launch and the coronal plasma evacuation are accompanied by the coronal shocks causing the radio bursts of type II, leave "footprints" in the form of EUV dimmings, and cause episodes of magnetic reconnection, which manifest themselves in radio emissions of accelerated electrons like the metric continuum and the low-frequency bursts of type III-l. In the 2000 July 14 event, the relativistic protons escape into the solar wind simultaneously with the coronal plasma evacuation. A possible interpretation of all this is that the high-energy protons of the PC are accelerated by coronal shock waves in high loops and then escape from these loops as the magnetic field opens up due to the CME-driven magnetic reconnection.

Similar to GLE 59, GLEs 60 and 65 started to rise during the metric type II bursts and EUV dimmings (Figure 4(a)), but the two GLEs began with EPC, in contrast to the short PC of GLE 59. The more prolonged rise of EPC compared to PC could be caused by the involvement of higher, probably the highest, coronal loops, where dekametric radio emissions could be produced. GLE 72 on 2017 September 10 comprises both weak PC and strong EPC (Figure 1). Only for that event are radio images available in the dekametric range (Morosan et al. 2019). The radio images at 30–50 MHz have revealed several sources of the type II emission accompanied by herringbone structures situated at different locations in the low corona within $\approx 35°$ of heliocentric angle from the eruption center (Morosan et al. 2019, Figure 5 therein). Those radio sources outline the coronal structure encountered by the shock. The total angular span of the structure associated with the EPC of GLE 72 was $\approx 70°$, which is comparable to the estimated size of the high-energy proton source of GLE 65 shown with the dashed circle in Figure 4(h).
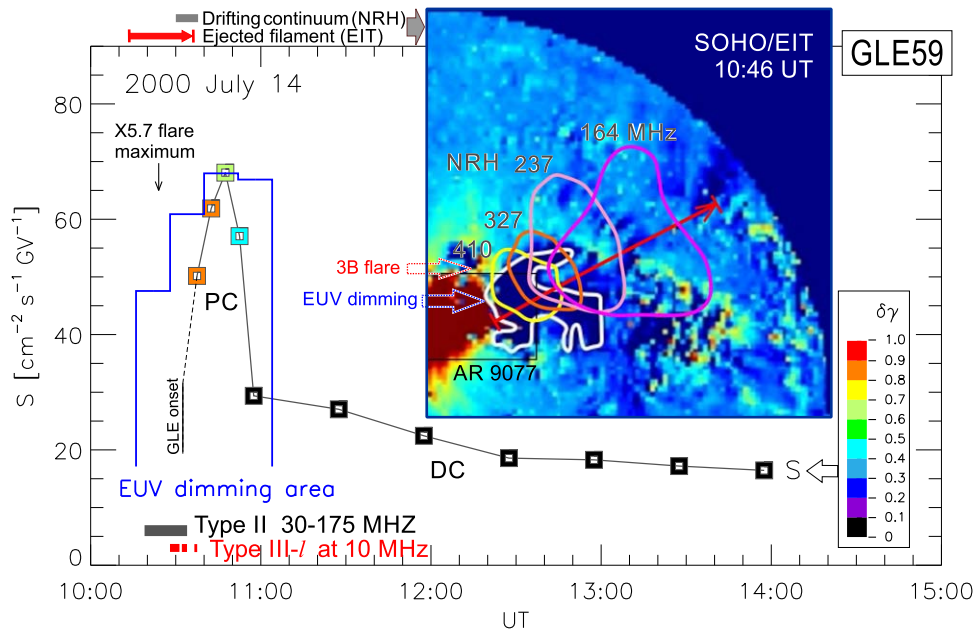
Figure 8. Time profile of the 1 GV proton flux of GLE 59 (points), including the PC peak and the DC. The histogram shows the coronal dimming area measured from the 195 Å fixed-difference images of the full solar disk by SoHO/EIT (plotted here in arbitrary units according to the NEMO catalog; Podladchikova & Berghmans 2005). The insert is the running difference image in 195 Å at the GLE maximum time, in a color scale that shows brightenings with colors from cyan to red, and dimmings in blue. The white contour in the insert outlines the northwestern dimming region. Additionally shown are contour plots of radio sources appearing sequentially at 410 MHz (10:30 UT; yellow), 327 MHz (orange), 237 MHz (pink), and 164 MHz (10:38 UT; magenta; NRH; Klein et al. 2001, Figure 7(a) therein). Similar to that figure, we also display the trajectory of a filament observed by SoHO/EIT (the red line with an arrow). The location of the optical 3B flare is also indicated. The two bars at the top of the figure show the time intervals during which successive images of the coronal filament (EIT) and the drifting-continuum radio sources (NRH) were taken. The bars at the bottom of the figure show the time interval of metric type II radio bursts registered at different ground-based observatories (30–175 MHz; Solar-Geophysical Data, nos. 672 and 673, part 1, 2000) and the time intervals of three low-frequency type III bursts observed by Wind/WAVES (type III-l according to the classification by Cane et al. (2002)). Note: the scatter-free transport time of GLE protons from the Sun to the Earth exceeds the flight time of light by ≈2.5 minutes, not accounted for in plotting.

Relativistic ions accelerated in the solar corona may precipitate back to the Sun, where they produce by nuclear interactions a number of secondaries, including neutrons, neutral pions, and thus the high-energy γ-rays from the pion decay. Detection of the neutral secondary emissions provides a tool for studying the acceleration and transport of high-energy ions at the Sun (Ramaty et al. 1987, 1993; Ryan 2000 and references therein). The high-energy γ-ray data are available for the 2003 October 28 event, and they indicate that protons and α particles with energies greater than 200 MeV nucleon^{-1} were already accelerated in the flare impulsive phase and were present through the end of the observation period at 11:13 UT (Kuznetsov et al. 2006; Trottet et al. 2008). The burst of γ-radiation with energy of 60–150 MeV consisted of a short pulse in the flare impulsive phase and a prolonged component that began between 11:04 UT and 11:06 UT, and exhibited a slow decay from 11:06:15 UT through the end of the observation period (Trottet et al. 2008, Figure 1 therein). By 11:06:15 UT, the Moreton wave observed in Meudon had traveled the distance of 0.43$R_\odot$–0.57 $R_\odot$, depending on the propagation direction (Muhr et al. 2010), being mostly inside the dashed circle shown in Figure 4(h). In addition, the NRH measurements at 411 MHZ at 11:03:01 UT and 11:03:11 UT show that the type II burst source was also inside that circle (Muhr et al. 2010). Hence, if the initial acceleration of the >200 MeV nucleon^{-1} ions was triggered by the shock, it occurred within the estimated source area of the GLE-producing protons, and it happened shortly before the GLE protons began to escape to the solar wind.

The steep rise of the GLE proton injection from the Sun began on 2003 October 28 at 11:09 UT (solar time plus eight minutes for a comparison with γ-ray observations at 1 au), when the interacting proton number was already gradually declining. Similar patterns were observed also in GLE 48 on 1990 May 24 and GLE 72 on 2017 September 10 (Kocharov et al. 1996a, 1996b, 2021). The prolonged component of the high-energy γ-ray emission could be produced by the accelerated ions trapped in high coronal loops and precipitating from there onto the Sun, while a fraction of the trapped protons may escape with some delay to 1 au to cause GLE. The spectral evolution observed in GLEs (the decrease of the spectral parameter $\delta\gamma$) is signature of a continual reacceleration of the trapped protons, like the stochastic reacceleration of the shock-accelerated particles downstream of the shock. Our results support the idea that the high-energy protons of the EPC of GLEs are accelerated by the flare eruption in large-scale coronal structures (not in flare loops), where they are further reaccelerated and from where they escape into the interplanetary medium during the magnetic field reconfiguration behind the CME.

7. Conclusions

For the first time, we have done and observed the following:

1. The net flux profiles of 15 newly fitted GLEs were plotted and compared, and two events of the same morphological type were selected for a detailed study, GLE 60 on 2001 April 15 and GLE 65 on 2003 October 28, both of which started with the extended PC emission.

2. Time profiles of four moments of the fitted distribution of the GLE-producing protons and the virtual 430 MeV proton channel were employed for a comparison of the two particle events.

3. The two GLEs had identical rise profiles of the proton flux up to and including the maximum and similar decay profiles, except the late decay phase.

4. In both events, the time interval between the emergence of the first 164 MHz source and the maximum of the soft X-ray flare was 8 minutes, and the relativistic proton flux reached its maximum after the next 43 ± 3 minutes (facts ①, ②, and ③, respectively).

5. In both events, the rise of the relativistic proton flux proceeded concurrently with irregular flashing of 164 MHz radio sources at different locations over the AR complex around the associated major solar flare.

6. In both events, at the end of the growth phase of the relativistic proton flux (the time ③), two 164 MHz sources were observed successively flashing at intervals of four minutes, in a few minutes after which all radio sources stabilized.

7. For the two selected events, the ratio of CME speeds and three ratios of the characteristic times of GLEs and soft X-ray flares coincided.

8. In the 2003 October 28 event, the flux of the GLE-producing protons and the deka-MeV proton flux arrived from essentially different directions.

9. In both events, periods of a strongly disturbed IMF were observed, in which the cross-field transport of high-energy protons prevailed.

10. In GLEs with a short PC, like GLE 59 on 2000 July 14, the time of the peak of the relativistic proton flux of the PC coincides with the peak time of the EUV dimming area.

The CMEs associated with GLE 60 and GLE 65 differed significantly in their speed far from the Sun and in the height at which the relativistic proton flux reached its maximum value, so they are unlikely to cause the observed similarity of the two GLEs. The rise time of the relativistic proton flux was the same in both events, as was the timescale of the global magnetic structure relaxation above the AR complex. The GLE decay times and the spectrum evolution rates are scaled with a factor of 2, associated with a difference in the flare pulse and CME launch. On the whole, the development of the two GLEs in their main phases, including the GLE's rise, maximum, and early decay, are completely controlled by the near-Sun eruption development and post-CME reorganization of large-scale coronal structures with a total size of $\approx 1 R_\odot$. In addition to the source of relativistic protons, other sources emit sub-relativistic electrons, relativistic electrons, and the two components of deka-MeV nucleon^{-1} ions.

Appendix
Solar Proton Distributions of GLE 60 and GLE 65

The NM network data analysis is based on the ideas originally formulated by Shea & Smart (1982), Cramp et al. (1997), Vashenyuk et al. (2006), and Bombardieri et al. (2007). It comprises a determination for each NM station of the rigidity-dependent asymptotic viewing directions and the rigidity cutoff by the modeling of particle propagation in the magnetosphere, and then a modeling of the solar particle interaction with the Earth's atmosphere, where secondary particles are produced to be detected by the ground-based detectors. An inverse method shall be applied for a derivation of the solar particle energy spectrum and pitch-angle distribution outside the magnetosphere.

We perform the NM signal modeling with the use of a newly computed and verified altitude-dependent NM yield function (Mishev et al. 2020). The model distribution of solar protons is given by Equation (1). The adopted inverse method is described elsewhere (Mishev et al. 2022 and references therein). As the main criterion of the goodness of the data fit, we adopt the sum of the squared differences between the observed relative NM increases $(\Delta N_i/N_i)_{\text{obs.}}$ and the modeled increases $(\Delta N_i/N_i)_{\text{mod.}}$ over all the m stations, from $i = 1$ to $i = m$; N_i is the pre-GLE background and ΔN_i is the GLE increase at the station i. More precisely, we consider the normalized square root of the sum (Himmelblau 1972; Dennis & Schnabel 1996; Mishev & Usoskin 2018):

$$\mathcal{D} = \frac{\sqrt{\sum_{i=1}^{m}[(\Delta N_i/N_i)_{\text{obs.}} - (\Delta N_i/N_i)_{\text{mod.}}]^2}}{\sum_{i=1}^{m}(\Delta N_i/N_i)_{\text{obs.}}}, \qquad (A1)$$

which shall be minimized. In moderately strong and strong events, a robust solution can be typically achieved with $\mathcal{D} \leqslant 5\%-10\%$. The $\mathcal{D}$-minimization criterion is used jointly with a few additional criteria: the difference between the observed and modeled NM increases at each station must be smaller or about 10%–15%; a number of positive residuals shall be nearly equal to the number of negative residuals; and the value of the reduced chi-squared, $\chi_r^2 = \chi^2/\text{DoF}$, shall be close to unity, where DoF is the number of degrees of freedom. This criteria set allows one to select a most relevant solution (Mishev et al. 2021). The fitting results for GLE 60 and GLE 65 are given respectively in Tables 1 and 2.

Table 1
Spectral and Angular Parameters of GLE 60 on 2001 April 15

Time Interval Minutes after 13:40 UT	j_o (m^{-2}s^{-1}sr^{-1}GV^{-1})	γ	$\delta\gamma$	σ^2 (rad^2)	ψ_{GSE} (deg)	λ_{GSE} (deg)	$\mathcal{D}$ %	χ_r^2
20–25	4.3E+05	4.64	0.7	2.5	−39	−33	8.8	1.1
25–30	4.8E+05	4.7	0.5	2.8	−39	−29	9.1	1.15
30–35	6.5E+05	4.72	0.45	3.1	−34	−30	8.2	1.1
35–40	7.3E+05	4.75	0.4	3.4	−31	−29	8.1	1.1
40–45	8.1E+05	4.8	0.37	3.7	−34	−33	7.2	1.05
45–50	8.9E+05	4.9	0.35	3.9	−34	−29	6.1	1.05
50–55	1.1E+06	4.9	0.33	3.9	−28	−29	5.5	1.0
55–60	1.0E+06	4.95	0.31	3.95	−27	−28	5.2	0.95
60–65	9.9E+05	5.0	0.31	4.0	−24	−27	5.1	0.99
65–70	9.9E+05	5.1	0.3	4.1	−22	−19	4.9	0.99
70–75	9.5E+05	5.2	0.3	4.3	−25	−19	5.0	0.98
80–85	8.6E+05	5.32	0.26	5.1	−31	−25	4.8	0.95
90–95	8.3E+05	5.36	0.25	5.3	−21	−28	4.9	0.96
100–105	8.1E+05	5.45	0.23	6.0	−11	−37	4.1	0.97
110–115	7.8E+05	5.5	0.2	7.5	−7	−64	4.0	0.96
120–125	7.7E+05	5.7	0.17	9.5	−6	−72	4.5	0.96
130–135	7.4E+05	6.0	0.13	11.5	−2	−73	3.3	0.99
140–145	7.2E+05	6.1	0.12	12.4	−1	−71	3.5	1.0
150–155	6.9E+05	6.15	0.11	13.1	−3	−72	3.4	0.97
160–165	6.6E+05	6.25	0.11	14	0	−74	3.6	0.98
170–175	6.3E+05	6.35	0.1	15.1	4	−79	3.6	0.99
180–185	6.3E+05	6.42	0.1	15.3	5	−84	3.8	0.97
190–195	5.9E+05	6.47	0.07	15.7	4	−87	3.4	0.96
200–205	5.2E+05	6.53	0.05	16.5	6	−89	3.7	0.99
210–215	4.9E+05	6.61	0.03	17	5	−88	3.9	0.98
220–225	4.6E+05	6.7	0.02	17	1	−85	4.5	1.03
230–235	4.2E+05	6.8	0.01	17	1	−89	4.1	0.99
240–245	3.9E+05	6.85	0.0	17.5	−2	−90	4.4	1.03
250–255	3.6E+05	6.9	0.0	17.5	−3	−88	4.5	1.04
260–275	3.4E+05	7.0	0.0	18	−2	−85	5.2	1.05
290–305	3.0E+05	7.2	0.0	18	−5	−81	6.1	1.1
320–335	2.7E+05	7.25	0.0	19	−8	−75	6.4	1.1
350–365	2.5E+05	7.26	0.0	19	−7	−66	6.3	1.1

Notes. The fitting parameters j_o, γ, $\delta\gamma$, and σ^2 are defined by Equation (1). The GSE coordinate angles, latitude ψ_{GSE} and longitude λ_{GSE}, are for the symmetry axis direction of the proton intensity distribution (antiparallel to the proton flux direction). The fit quality parameters $\mathcal{D}$ and χ_r^2 are defined in the Appendix.

Table 2
Spectral and Angular Parameters of GLE 65 on 2003 October 28

Time Interval Minutes after 11:00 UT	j_o (m^{-2}s^{-1}sr^{-1}GV^{-1})	γ	$\delta\gamma$	σ^2 (rad^2)	ψ_{GSE} (deg)	λ_{GSE} (deg)	$\mathcal{D}$ %	χ_r^2
25–30	1.5E+05	4.68	0.38	1.3	−63	168	12.2	1.02
30–35	2.0E+05	4.72	0.31	1.45	−57	172	11.2	1.02
35–40	2.2E+05	4.75	0.28	1.52	−61	161	10.2	1.02
40–45	2.4E+05	4.79	0.26	1.55	−71	124	9.0	1.01
45–50	2.8E+05	4.8	0.25	1.7	−69	131	8.9	1.01
50–55	3.3E+05	4.81	0.25	1.8	−67	138	8.8	1.01
55–60	3.2E+05	4.85	0.25	1.95	−70	136	9.2	1.02
60–65	3.0E+05	4.96	0.22	2.1	−79	154	8.2	1.01
65–70	3.0E+05	5.23	0.2	2.5	−67	165	8.5	1.02
75–80	2.9E+05	5.53	0.17	2.55	−62	179	9.0	1.02
85–90	3.0E+05	5.73	0.03	2.85	−45	−174	6.5	1.01
95–100	3.0E+05	5.74	0.02	2.9	−47	−177	7.5	1.05
105–110	2.8E+05	5.95	0.01	3.8	−43	−178	6.1	1.01
115–120	2.8E+05	5.9	0.0	4.3	−49	−176	6.0	1.0
125–130	2.7E+05	6.18	0.0	4.5	−47	−168	5.6	1.0
135–140	2.7E+05	6.2	0.0	4.55	−51	−172	5.8	0.99
145–150	2.7E+05	6.2	0.0	4.55	−55	−171	6.2	0.97
155–160	2.7E+05	6.22	0.0	4.7	−54	−164	5.1	0.98
165–170	2.7E+05	6.23	0.0	5.1	−58	−164	5.5	1.0

Table 2
(Continued)

Time Interval Minutes after 11:00 UT	j_o (m^{-2}s^{-1}sr^{-1}GV^{-1})	γ	$\delta\gamma$	σ^2 (rad^2)	ψ_{GSE} (deg)	λ_{GSE} (deg)	$\mathcal{D}$ %	χ_r^2
175–180	2.7E+05	6.24	0.0	5.3	−61	−160	5.7	0.99
185–190	2.7E+05	6.26	0.0	5.5	−57	−153	5.7	0.99
195–200	2.6E+05	6.27	0.0	5.6	−59	−153	5.8	0.99
205–210	2.6E+05	6.3	0.0	5.7	−58	−149	5.8	0.98
215–220	2.6E+05	6.32	0.0	5.8	−56	−146	5.8	0.98
225–230	2.5E+05	6.33	0.0	5.9	−60	−143	5.8	0.98
235–240	2.5E+05	6.37	0.0	6.0	−59	−139	5.9	1.01
255–260	2.5E+05	6.42	0.0	6.3	−57	−127	5.7	0.98
270–275	2.5E+05	6.44	0.0	6.5	−58	−123	5.7	0.99
285–290	2.5E+05	6.47	0.0	6.7	−59	−119	5.8	1.01
300–305	2.5E+05	6.5	0.0	7.1	−61	−112	6.2	1.03
330–335	2.5E+05	6.5	0.0	7.2	−56	−99	6.2	1.04
360–365	2.5E+05	6.55	0.0	7.4	−59	−89	6.5	1.03

Notes. The fitting parameters j_o, γ, $\delta\gamma$, and σ^2 are defined by Equation (1). The GSE coordinate angles, latitude ψ_{GSE} and longitude λ_{GSE}, are for the symmetry axis direction of the proton intensity distribution (antiparallel to the proton flux direction). The fit quality parameters $\mathcal{D}$ and χ_r^2 are defined in the Appendix.

ORCID iDs

Leon Kocharov ⬢ https://orcid.org/0000-0002-2077-5618
Rami Vainio ⬢ https://orcid.org/0000-0002-3298-2067
Ilya Usoskin ⬢ https://orcid.org/0000-0001-8227-9081

References

Attrill, G., Nakwacki, M. S., Harra, L. K., et al. 2006, SoPh, 238, 117
Ashfield, W., & Longcope, D. 2023, ApJ, 944, 147
Aurass, H., Mann, G., Rauscher, G., & Warmuth, A. 2006, A&A, 457, 681
Bieber, J. W., & Evenson, P. A. 1995, in Proc. XXIV Internat. Cosmic Ray Conf., ed. N. Iucci & E. Lamanna (Rome: IUPAP), 1316
Bombardieri, D. J., Michael, K. J., Duldig, M. L., & Humble, J. E. 2007, ApJ, 665, 813
Bougeret, J. L., et al. 1995, SSRv, 71, 231
Brueckner, G. E., et al. 1995, SoPh, 162, 357
Cane, H. V., Erickson, W. C., & Prestage, N. P. 2002, JGR, 107, 1315
Cane, H. V., & Richardson, I. G. 2003, JGRA, 108, 1156
Clem, J., & Dorman, L. 2000, SSRv, 93, 335
Cramp, J. L., Duldig, M. L., Flückiger, et al. 1997, JGRA, 102, 24237
Debrunner, H., & Brunberg, E. 1968, CaJPh, 46, 1069
Debrunner, H., & Lockwood, J. A. 1980, JGR, 85, 6853
Delaboudiniere, J.-P., Artzner, G. E., Brunaud, J., et al. 1995, SoPh, 162, 291
Dennis, J. E., & Schnabel, R. B. 1996, Numerical Methods for Unconstrained Optimization and Nonlinear Equations (Englewood Cliffs: Prentice-Hall)
Desorgher, L., Kudela, K., Flückiger, E. O., et al. 2009, AcGeo, 57, 75
Dorman, L. 2004, Cosmic Rays in the Earth's Atmosphere and Underground, Astrophysics and Space Science Library (Dordrecht: Kluwer Academic), 303
Gopalswamy, N., Mäkela, P., & Yashiro, S. 2019, SunGe, 14, 111
Hatton, C. 1971, Progress in Elementary Particle and Cosmic-ray Physics X (Amsterdam: North Holland Publishing Co.), 1
Himmelblau, D. M. 1972, Applied Nonlinear Programming (New York: McGraw Hill)
Hovestadt, D., Hilchenbach, M., Bürgi, A., et al. 1995, SoPh, 162, 441
Jiricka, K., Karlicky, M., Kepka, O., & Tlamicha, A. 1993, SoPh, 147, 203
Kahler, S. W., & Ling, A. G. 2022, ApJ, 934, 175
Kerdraon, A., & Delouis, J. M. 1997, in Coronal Physics from Radio and Space Observations, ed. G. Trottet, 483 (Berlin: Springer), 192
Klassen, A., Krucker, S., Kunow, H., et al. 2005, JGRA, 110, A09S04
Klein, K.-L., Trottet, G., Lantos, P., & Delaboudinière, 2001, A&A, 373, 1082
Kocharov, L., Omodei, N., Mishev, A., et al. 2021, ApJ, 915, 12
Kocharov, L., Pesce-Rollins, M., Laitinen, T., et al. 2020, ApJ, 890, 13
Kocharov, L., Torsti, J., Vainio, R., Kovaltsov, G., & Usoskin, I. 1996a, SoPh, 169, 181
Kocharov, L., Kovaltsov, G., Torsti, J., et al. 1996b, in AIP Conf. Proc. 374, High Energy Solar Physics, ed. R. Ramaty, N. Mandzhavidze, & X.-M. Hua (New York: AIP), 246
Krucker, S., Larson, D. E., Lin, R. P., & Thompson, B. J. 1999, ApJ, 519, 864
Kuznetsov, S. N., Kurt, V. G., Myagkova, I. N., Yushkov, B. Y., & Kudela, K. 2006, SoSyR, 40, 104
Laitinen, T., & Dalla, S. 2017, ApJ, 834, 124
Marsh, M. S., Dalla, S., Kelly, J., & Laitinen, T. 2013, ApJ, 774, 4
Mészárosová, H., Karlický, M., Rybák, J., Fárník, F., & Jiřička, K. 2006, A&A, 460, 865
Miroshnichenko, L. I., Klein, K.-L., Trottet, G., et al. 2005, JGRA, 110, A11S90
Mishev, A., Kocharov, L., Koldobskiy, S., et al. 2022, SoPh, 297, 88
Mishev, A., Koldobskiy, S., Kocharov, L., & Usoskin, I. 2021, SoPh, 296, 79
Mishev, A., Koldobskiy, S., Kovaltsov, G., Gil, A., & Usoskin, I. 2020, JGRA, 125, e2019JA027433
Mishev, A., & Usoskin, I. 2013, JPhCS, 409, 012152
Mishev, A., & Usoskin, I. 2018, SpWea, 16, 1921
Morosan, D. E., Carley, E. P., Hayes, L. A., et al. 2019, NatAs, 3, 452
Muhr, H., Vršnak, B., Temmer, M., Veronig, A. M., & Magdalenić, J. 2010, ApJ, 708, 1639
Nitta, N. V., DeRosa, M. L., & Nightingale, R. W. 2012, SSRv, 171, 61
Park, J., Innes, D. E., Bucik, R., & Moon, Y.-J. 2013, ApJ, 779, 184
Pizzo, V. J., Hill, S.-M., Balch, C. C., et al. 2005, SoPh, 226, 283
Podladchikova, O., & Berghmans, 2005, SoPh, 228, 265
Ramaty, R., Mandzhavidze, N., Kozlovsky, B., & Skibo, J. G. 1993, AdSpR, 13, 275
Ramaty, R., Murphy, R. J., & Dermer, C. D. 1987, ApJL, 316, L41
Richardson, I. G., & Cane, H. V. 2010, SoPh, 264, 189
Ryan, J. 2000, SSRv, 93, 581
Shea, M. A., & Smart, D.-F. 1982, SSRv, 32, 251
Smith, C. W., et al. 1998, SSRv, 86, 613
Thompson, B. J., Plunkett, S. P., Gurman, J. B., et al. 1998, GeoRL, 25, 2465
Torsti, J., Kocharov, L. G., Teittinen, M., & Thompson, B. J. 1999, ApJ, 510, 460
Torsti, J., Valtonen, E., Lumme, M., et al. 1995, SoPh, 162, 505
Trottet, G., Krucker, S., Lüthi, T., & Magun, A. 2008, ApJ, 678, 509
Van Hollebeke, M. A. I. 1975, in Proc. XIV Internat. Cosmic Ray Conf., ed. K. Pinkau (Munich: Max Planck), 1563
Vashenyuk, E. V., Balabin, Y. V., Perez-Peraza, J., Gallegos-Cruz, A., & Miroshnichenko, L. I. 2006, AdSpR, 38, 411
Vashenyuk, E. V., Miroshnichenko, L. I., Perez-Peraza, J., Kananen, H., & Tanskanen, P. 1997, in Proc. XXV Internat. Cosmic Ray Conf., ed. M. S. Potgieter, C. Raubenheimer, & D. J. van der Walt (Potchefstroom: Potchefstroom Univ.), 1
Yashiro, S., et al. 2004, JGR, 109, A07105